ACS OMEGA

http://pubs.acs.org/journal/acsodf

Article

Theoretical Study on the Carrier Mobility and Optical Properties of $CsPbI_3$ by DFT

Li-Ke Gao and Yan-Lin Tang*

Cite This: *ACS Omega* 2021, 6, 11545−11555

Read Online

ACCESS | Metrics & More | Article Recommendations

ABSTRACT: The advantages of organic−inorganic hybrid halide perovskites and related materials, such as high absorption coefficient, appropriate band gap, excellent carrier mobility, and long carrier life, provide the possibility for the preparation of low-cost and high-efficiency solar cell materials. Among the inorganic materials, $CsPbI_3$ is paid more attention to by researchers as $CsPbI_3$ has incomparable advantages. In this paper, based on density functional theory (DFT), we first analyze the crystal structure, electronic properties, and work function of two common bulk structures of $CsPbI_3$ and their slices, and then, we study the carrier mobility, exciton binding energy, and light absorption coefficient. Considering that $CsPbI_3$ contains heavy elements, the spin−orbit coupling (SOC) effect was also considered in the calculation. The highest mobility is that electrons of the cubic structure reach 1399 $cm^2\ V^{-1}\ S^{-1}$ after considering the SOC effect, which is equal to that of traditional solar cells (such as Si-based, PbSe, and PbTe). The lowest exciton binding energy is 101 meV in the cubic bulk structure, which is beneficial to the separation of photogenerated carriers. In the visible region, the absorption coefficient of the cubic structure is the best among all structures, reaching $10^5\ cm^{-1}$. Through the study of mobility, exciton binding energy, and light absorption coefficient, it is found that the cubic bulk structure in all structures of $CsPbI_3$ has the best photoelectric performance. This paper can provide some guidance for the experimental preparation of $CsPbI_3$ as a potential high-efficiency solar cell material.

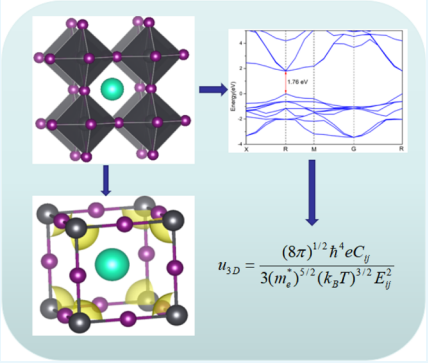

1. INTRODUCTION

With the continuous growth of the world's population and the increasing demand for energy, the problem of energy shortage is becoming more and more serious. Therefore, it is extremely urgent to find a new kind of renewable and pollution-free energy, and solar cells have become one of the first choices.[1−9] The first generation of solar cells was developed in the 1970's, mainly composed of monocrystalline silicon, which was quickly applied due to its excellent stability and extensive material acquisition. However, the price is very expensive due to the high purity requirement of silicon in the preparation process. Moreover, because silicon is an indirect band gap semiconductor, the absorption efficiency of sunlight is not very high, which limits the carrier transmission to some extent. Theoretical calculations show that the maximum carrier mobility of Si-based solar cell materials is 1400 $cm^2\ V^{-1}\ S^{-1}$,[10] and the conversion efficiency of solar cells is still not very high after decades.[11−13] The second generation of solar cells was developed in the 1980's, mainly using amorphous silicon as the raw material of thin-film solar cells. Although they are simple and flexible, their efficiency is still not high, so the market is still dominated by the first generation.[14,15] In order to find a kind of efficient and stable solar cell materials, the third generation solar cells came into being in the 1990's, among which the perovskite belongs to the third generation. In 2009, Kojima *et al.*[16] first prepared perovskite-type organic−inorganic hybrid materials instead of organic molecules as light-absorbing materials for solar cells (the efficiency was 3.8%). The U.S. National Renewable Energy Laboratory released a single section regarding a perovskite solar cell with a certified maximum efficiency of 25.5% in 2020.[17] In the past ten years, organic−inorganic hybrid halide perovskites and related materials have provided the possibility to prepare low-cost and high-efficiency solar cell materials due to their advantages such as high absorption coefficient, appropriate band gap, excellent carrier mobility, and long carrier life.[18−22] Perovskites with an ABX_3 structure has attracted many researchers because of their efficient light absorption performance,[23−26] where A is an organic−inorganic cation such as FA (FA = formamidinium, NH_2CHNH_2), MA (MA = methylammouium, CH_3NH_3), or Cs, B is a metal ion such as Pb, Sn, or Ge, and X is a halide anion. In the ABX_3 structure of the

Received: February 9, 2021
Accepted: April 6, 2021
Published: April 19, 2021

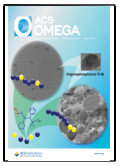

organic−inorganic hybrid perovskite cells generally the metal atoms are located at the core of the octahedron, the halogen atoms are located at the top corner of the octahedron, and the organic−inorganic molecules are located at the top corner of the face-centered cubic lattice. The octahedron of $[BX_6]$ is composed of three-dimensional shapes with a co-vertex connection. According to Pauling's connection rule of ligand polyhedron,[27] a co-planar or co-edge connection will reduce the distance between atoms, which increases the repulsive force between ions with the same electric polarity and reduces the stability of the structure, so the co-vertex is more stable. In addition, the co-vertex connection structure makes the gap of the octahedral meshes larger than the gap between the co-edge and co-planar structures, allowing larger size ions to fill in. In general, the most commonly used ABX_3 perovskite materials will choose organic $MAPbI_3$ and $FAPbI_3$ for their excellent photoelectric conversion efficiency. However, the organic cations MA^+ and FA^+ are easy to decompose because of the lengthy exposure to the humid environment. At present, all inorganic perovskites have attracted people's attention, among which the perovskite of the $CsPbI_3$ series has been studied most. $CsPbI_3$ has a variety of phases. It forms into a black phase for which the space groups are $Pm\bar{3}m$, $P4/mbm$, and *Pnma* at high temperatures, and it forms into a yellow phase for which the space group is *Pnma* at low temperatures.[28] The challenge now is how to form a stable black phase $CsPbI_3$ at room temperature[29,30] because the black phase (cubic structure) has a band gap of 1.73 eV, which is ideal to make perovskite-Si heterojunction solar cell material.[31] Many researchers report that a stable black phase can only form above 300 °C.[32,33] However, Eperon *et al.* reported that by careful processing control and development of a low-temperature phase transition route, they had obtained a stable $CsPbI_3$ of the black perovskite phase at room temperature.[31] Later, Hoffman *et al.* also synthesized cubic $CsPbI_3$ at low temperatures through a halide exchange reaction using films of sintered $CsPbBr_3$ nanocrystals.[34] In 2019, Steele *et al.* reported the use of substrate clamping and biaxial strain to render the black-phase $CsPbI_3$ thin films stable at room temperature.[35] The preparation of stable $CsPbI_3$ at room temperature made it possible to study its numerous properties.

The carrier mobility in two-dimensional photoelectric materials has attracted many researchers, such as Qiao *et al.* studied the carrier mobility in black phosphorus of single-layer and multilayer; Xie *et al.* studied the carrier mobility in BC_2N, and they have confirmed that these materials have good photoelectric properties through the density functional theory (DFT).[36−38] The carrier mobility of three-dimensional crystal materials has also attracted many researchers, such as Jong *et al.* found that the mobilities of $CsGeX_3$ were 1677, 1401, and 863 $cm^2\ V^{-1}\ S^{-1}$ for the X = I, Br, and Cl at 300 K.[39] Wang *et al.* found that the electron and hole mobilities of $MAPbI_3$ could reach surprisingly high values of $7-30 \times 10^3$ and $1.5-5.5 \times 10^3$ $cm^2\ V^{-1}\ S^{-1}$, but both are estimated to be much higher than the current experimental measurements.[40] Ying *et al.* found that the electron and hole mobilities of the cubic structure of $CsPbI_3$ were 430 and 2820 $cm^2\ V^{-1}\ S^{-1}$.[41] Lee studied the relationship between mechanical stability and charge mobility in the MA-based hybrid Perovskites and optimized the charge mobility by adjusting its structure.[42] Poncé *et al.* demonstrate that low-energy longitudinal optical phonons associated with the fluctuations of the Pb−I bonds of halide perovskites ultimately limit the mobility to 80 $cm^2\ V^{-1}\ S^{-1}$ at room temperature.[43]

Due to the complexity to study the property of perovskite's mobility, it has been paid much attention to by researchers. In this paper, based on DFT, we first analyzed the crystal structure, electronic properties, and work function of the two common bulk structures of $CsPbI_3$ and their slices, and then, we studied the carrier mobility, exciton binding energy, and light absorption coefficient. The research work in this paper provides a theoretical basis for $CsPbI_3$ to become a potential high-efficiency solar cell material and a certain guiding role for the preparation of later experiments.

2. COMPUTATIONAL METHODS

The DFT is calculated by using the augmented wave method realized in Vienna *ab initio* simulation package.[44] The methods of projector augmented wave using the norm-conserving pseudo-potentials[45] for Cs, Pb, and I atoms were treated to understand the electrostatic interactions between valence and core electrons. The generalized gradient approximation (GGA) of the Perdew−Burke−Ernzerhof (PBE) functional was depicted during geometry optimization and electronic structure calculation.[46] In order to correct the underestimation of band gap by PBE, we also used a Heyd−Scuseria−Ernzerhof in 2006 (HSE06) hybridization functional to correct it. Because $CsPbI_3$ contains the heavy elements Pb and I, the spin−orbit coupling (SOC) effect cannot be ignored in the calculation of the band structure.[47,48] The calculated valence electrons of each atom are as follows: 9 for Cs-$5s^2 5p^6 6s^1$, 4 for Pb-$6s^2 6p^2$, and 7 for I-$5s^2 5p^5$. The *k*-point grid of the bulk is set as $5 \times 5 \times 5$, and the *k*-point of (1 0 0), (0 1 0), (0 0 1), and (1 1 1) surfaces is set as $5 \times 5 \times 1$. The lattice parameters and atomic positions are fully relaxed until the Hellmann−Feynman force on each atom is less than 0.005 eV/Å. The plane-wave cutoff energy is set to 450 eV, and the self-consistent field calculation was considered to be converged when the total energy difference was less than 1×10^{-5} eV.

In inorganic semiconductors, the coherent wavelength of thermally activated electrons or holes is much longer than the lattice constant at room temperature and close to the wavelength of phonons. The electron acoustic phonon coupling, leading to scattering in the low-energy region,[49,50] can be attained based on the deformation potential (DP) theory, which was first proposed by Bardeen and Shockley.[51] According to the DP theory, we can get carrier mobility μ in 2D[10] materials from the following expression

$$u_{2D} = \frac{e\hbar^3 C_{2D}}{k_B T m_e^* m_d (E_1^i)^2} \quad (1)$$

where e is the electronic charge, $\hbar$ is the reduced Planck constant, k_B is the Boltzmann constant, and T is the room temperature (T = 300 K). m_e^* is the effective mass, we can calculate it by the finite difference method using the equation $m_e^* = \hbar^2/(\partial^2 E(k)/\partial k^2)$, where E_k are the band-edge eigenvalues and k is the wave vector. m_d is the average effective mass determined by $m_d = \sqrt{m_x^* m_y^*}$. E_1 is the DP constant of the valence band maximum (VBM) for the hole or conduction band minimum (CBM) for the electron along the transport direction, which was defined as $E_1^i = \Delta E_i/(\Delta l/l_0)$. Here, ΔE_i is the energy change of the *i*th band under an appropriate unit compression or expansion (calculated at 0.5%

https://doi.org/10.1021/acsomega.1c00734
ACS Omega 2021, 6, 11545−11555

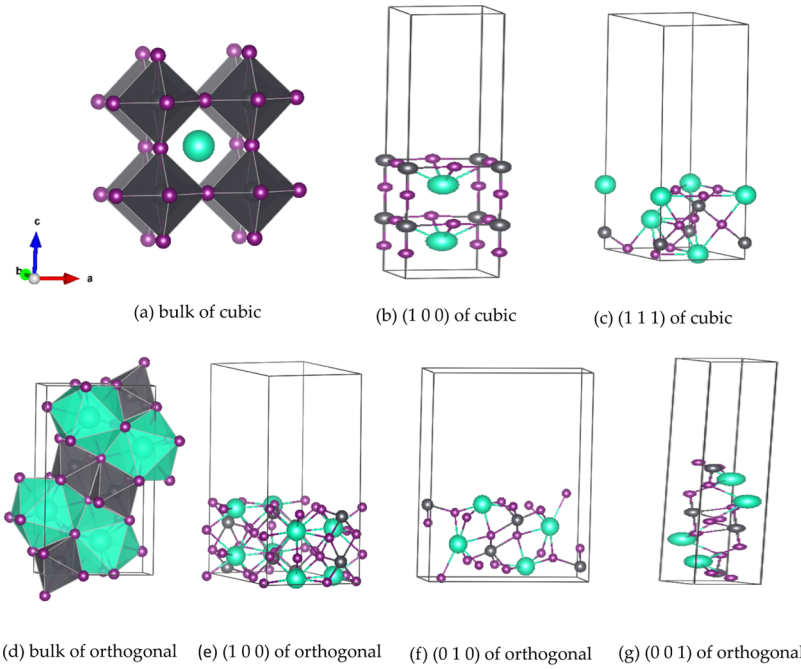

Figure 1. Crystal structures and sliced models of $CsPbI_3$. Green-, gray-, and purple-colored balls represent the Cs, Pb, and I atoms.

Table 1. Crystal and Slice Constants after Geometry Optimization and Experimental Data

original crystal	a (Å)	b (Å)	c (Å)	α (deg)	β (deg)	γ (deg)	V (Å^3)	space group	crystal system
bulk of cubic	6.38	6.38	6.38	90	90	90	260	$Pm\bar{3}m$	cubic
experiment[52]	6.29	6.29	6.29				249		
bulk of orthogonal	10.95	5.05	18.51	90	90	90	1019	*Pnma*	orthogonal
experiment[53]	9.02	8.69	12.55				984		
(1 0 0) of cubic	6.27	6.27	29.60	90	90	90	1164		
(1 1 1) of cubic	8.67	8.67	26.72	90	90	120	2009		
(1 0 0) of orthogonal	10.70	18.20	27.75	90	90	90	5404		
(0 1 0) of orthogonal	19.27	4.98	28.33	90	90	90	2719		
(0 0 1) of orthogonal	5.11	9.66	35.32	90	90	90	1743		

step size), l_0 is the lattice constant in the direction of the transport, and Δl is the deformation of l_0. The elastic modulus C_{2D} in the propagation direction can be obtained from $2(E - E_0)/S_0 = C_{2D}(\Delta l/l_0)^2$, where E is the total energy and S_0 is the lattice area at equilibrium for a 2D system.[34] It is noticed that formula 1 represents a phonon-limited scattering model.[38]

We can also get the charge carrier mobility of the crystal from the following formula[51]

$$u_{3D} = \frac{(8\pi)^{1/2}\hbar^4 eC_{ij}}{3(m_e^*)^{5/2}(k_B T)^{3/2}E_{ij}^2} \quad (2)$$

The physical quantity above is the same as formula 1, but it should be noted that the elastic modulus and the DP constant are calculated in a slightly different way. C_{ij} can be obtained directly by calculating the elastic properties. E_{ij} is defined by $E_{ij} = \Delta E_{ij}/(\Delta V/V_0)$; here, ΔV is the deformation of a crystal under an appropriate unit compression or expansion and V_0 is the lattice volume at equilibrium for a 3D system.

3. RESULTS AND DISCUSSION

3.1. Structure Properties. $CsPbI_3$ mainly exists in two phases, which will undergo the corresponding phase transitions with the change of temperature. It is the yellow phase (orthogonal structure and space group is *Pnma*) at room temperature and will translate into the black phase (cubic structure and space group is $Pm\bar{3}m$) above 310 °C.[28] Figure 1 shows crystal structures and sliced models of $CsPbI_3$, in which Figure 1a,d are the bulk diagrams of the cubic and orthogonal structures, and the rest are sliced models of the cubic and orthogonal structures. The reason for selecting these slices is that we used the morphology calculation function of Materials Studio and found that these slices had the greatest probability of existence (Morphology defines the probability based on the lowest energy and the maximum exposed surface area after being sliced). Table 1 shows the parameters after geometry optimization compared with the experimental data. The unit cell parameters used for theoretical calculations are obtained from Materials Project. Compared with the optimized unit cell parameters with the experimental data, there is little difference in the cubic structure, while the orthogonal structure is much different. The *c*-axis of the slice is the direction of the vacuum layer, and the thickness of the vacuum layer is all 20 Å.

3.2. Electronic Properties (Band and DOS). The band diagrams of the cubic and orthogonal structures of $CsPbI_3$ were calculated by using different exchange correlation functions of GGA−PBE and HSE06, respectively, as shown in Figure 2. It can be seen from the figure that the band gaps of the two structures calculated by PBE are 1.44 and 2.56 eV, while those calculated by HSE06 are 1.76 and 2.83 eV,

https://doi.org/10.1021/acsomega.1c00734
ACS Omega 2021, 6, 11545−11555

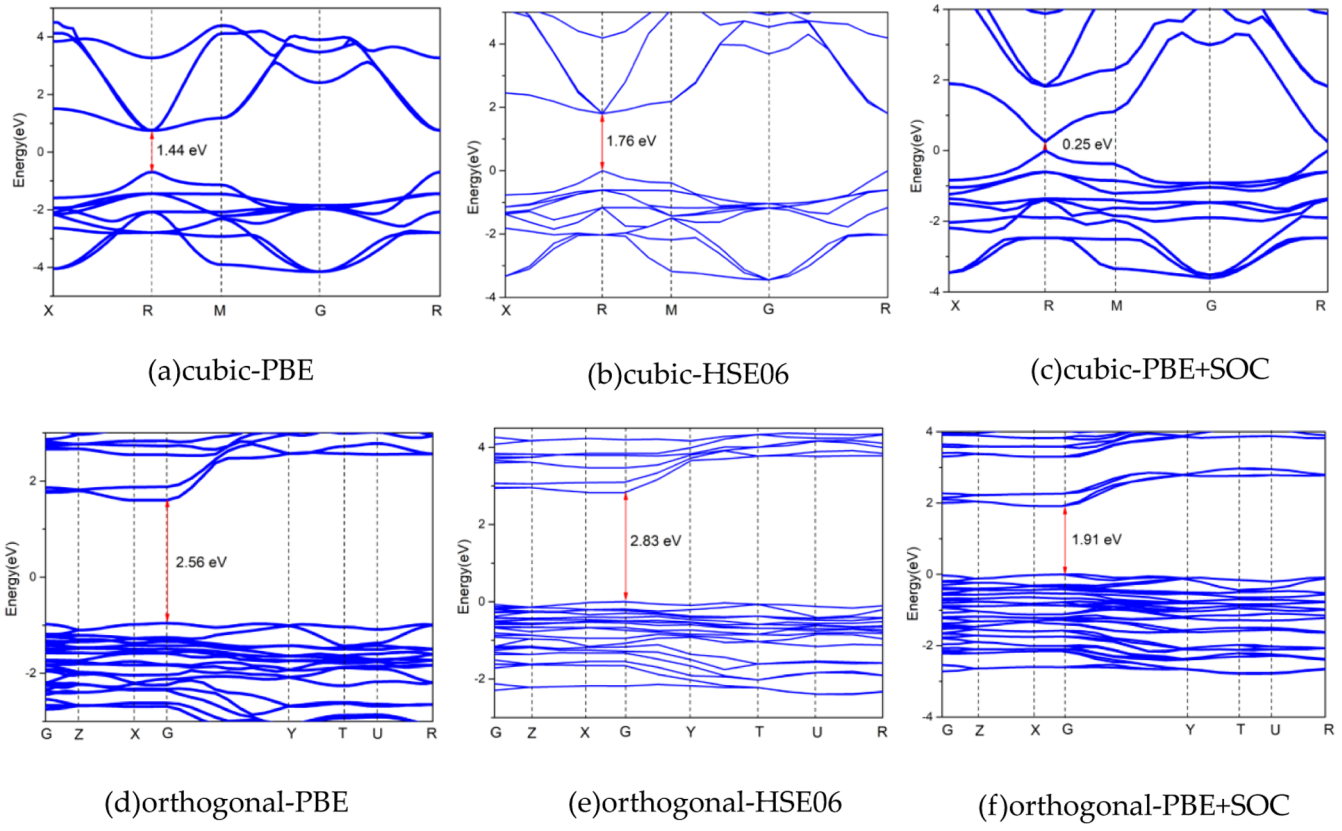

Figure 2. Band structures of the cubic and orthogonal phases of $CsPbI_3$ were calculated by PBE, HSE06, and PBE + SOC. The high symmetry points in the Brillouin zone of the cubic structure are along the directions of $X(0.5,0,0) \rightarrow R(0.5,0.5,0.5) \rightarrow M(0.5,0.5,0) \rightarrow G(0,0,0) \rightarrow R(0.5,0.5,0.5)$, and the orthogonal structure's high symmetry points are along directions of $G(0,0,0) \rightarrow Z(0,0,0.5) \rightarrow X(0.5,0,0) \rightarrow G(0,0,0) \rightarrow Y(0,0.5,0) \rightarrow T(-0.5,0.5,0) \rightarrow U(0,0.5,0.5) \rightarrow R(0.5,0.5,0.5)$.

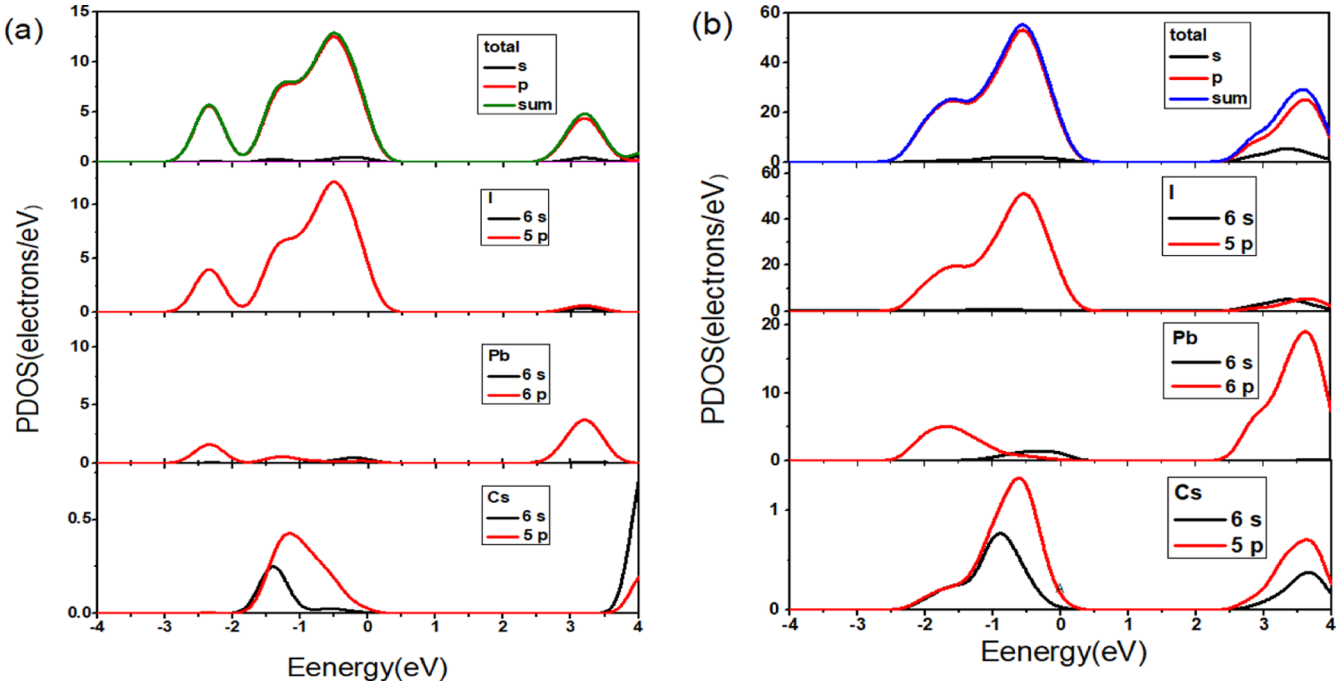

Figure 3. Partial DOS (PDOS) of the (a) cubic and (b) orthogonal structures of $CsPbI_3$.

respectively. We know that the experimental band gap for the cubic structure is 1.73 eV and that for the orthogonal structure is 2.82 eV.[28] The band gap calculated by PBE is underestimated, while the band gap calculated by HSE06 is close to the experimental value, which is consistent with the conclusion calculated by other research studies. Comparing the band

https://doi.org/10.1021/acsomega.1c00734
ACS Omega 2021, 6, 11545−11555

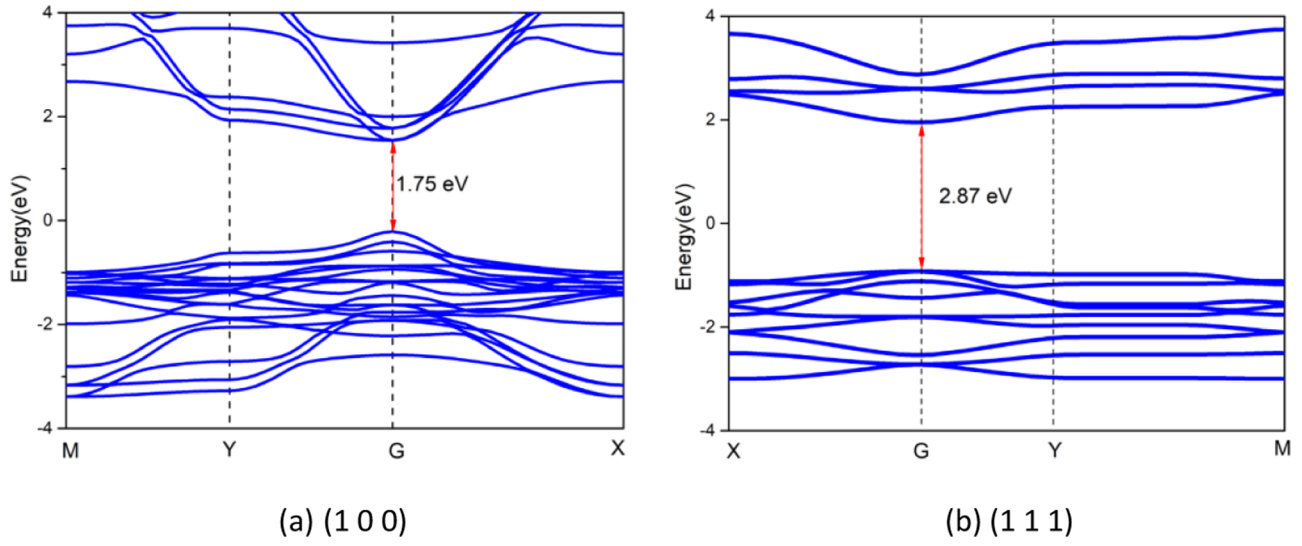

Figure 4. Band structures of (1 0 0) and (1 1 1) slices of the cubic phase of $CsPbI_3$. The high symmetry points in the Brillouin zone of slices of (1 0 0) and (1 1 1) are along directions of $M(0.5,0.5,0) \rightarrow Y(0,0.5,0) \rightarrow G(0,0,0) \rightarrow X(0.5,0,0)$, $X(0.5,0,0) \rightarrow G(0,0,0) \rightarrow Y(0,0.5,0) \rightarrow M(0.5,0.5,0)$ respectively.

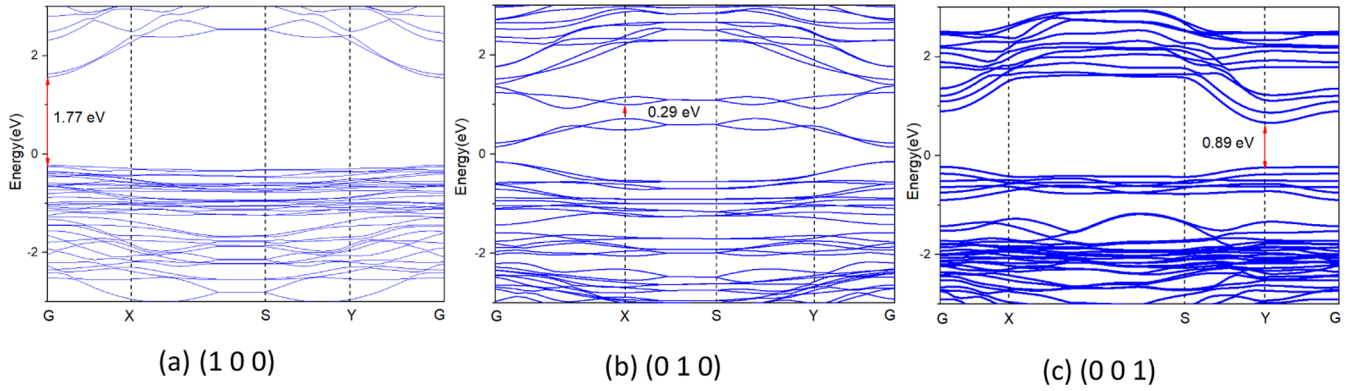

Figure 5. Band structures of (1 0 0), (0 1 0), and (1 1 1) slices of orthogonal phase of $CsPbI_3$. The high symmetry points in the Brillouin zone of slices of the orthogonal structure are all along directions of $G(0,0,0) \rightarrow X(0.5,0,0) \rightarrow S(0.5,0.5,0) \rightarrow Y(0,0.5,0) \rightarrow G(0,0,0)$.

structure diagram obtained by the two methods, we find that they are very close. As described in the literature,[47,54] the properties calculated by PBE are accurate and less time-consuming. Therefore, the subsequent studies in this paper are all based on the PBE calculation. Meanwhile, the band structure calculated by PBE + SOC is also plotted in Figure 2. After considering the SOC effect, the energy levels begin to split due to the relativistic effect. It can be seen from the band diagrams shown in Figure 2c,f that the splitting of CBM is more obvious.

Figure 3 shows the density of state (DOS) diagram of the cubic and orthogonal structures. According to the DOS diagram, the valence band of the two structures is mainly contributed by the I-5p states, while the conduction band is mainly contributed by the Pb 6p states. Cs atoms have little contribution to electrons near the Fermi surface, but they play an important role in the stability of the crystal structure. According to the Goldschmidt criterion,[55] $T = (R_A + R_X)/\sqrt{2}(R_B + R_X)$, the tolerance factor of $CsPbI_3$ is 0.81 which meets the stability conditions (the structure is stable when T is between 0.81 and 1.11[56]). The DOS of the orthogonal structure near the Fermi surface is significantly denser than that of the cubic structure. The maximum value of the orthogonal structure is 56 electrons/eV, while the maximum value of the cubic structure is only 13 electrons/eV. Combining with the band structure diagram shown in Figure 2, we find that the band localization of the orthogonal structure is obviously stronger, so the electrons are distributed more near the Fermi surface, but the overall distribution of DOS of the two structures is similar. The DOS of the orthogonal structure is higher than that of the cubic structure mainly because the size of the unit cell of the orthogonal structure used for the calculation is larger and the number of atoms is more than that of the cubic structure.

We cut the cubic structure to be (1 0 0), (0 1 0), (0 0 1), and (1 1 1) surfaces. As the symmetry of the crystal, the three surfaces (1 0 0), (0 1 0), and (0 0 1) are the same, so we only analyze the characteristics of (1 0 0) and (1 1 1) surfaces. At the same time, the orthogonal structures (1 0 0), (0 1 0), and (0 0 1) surfaces are cut and analyzed. Figures 4 and 5 show the band diagrams of the cubic and orthogonal structures after being sliced, respectively. It is found that the band gap of the cubic structure increases obviously, while the band gap of the orthogonal structure decreases significantly. We know that the crystal becomes thinner after being sliced, and the interaction between the atoms in the crystal becomes weaker, resulting in

https://doi.org/10.1021/acsomega.1c00734
ACS Omega 2021, 6, 11545−11555

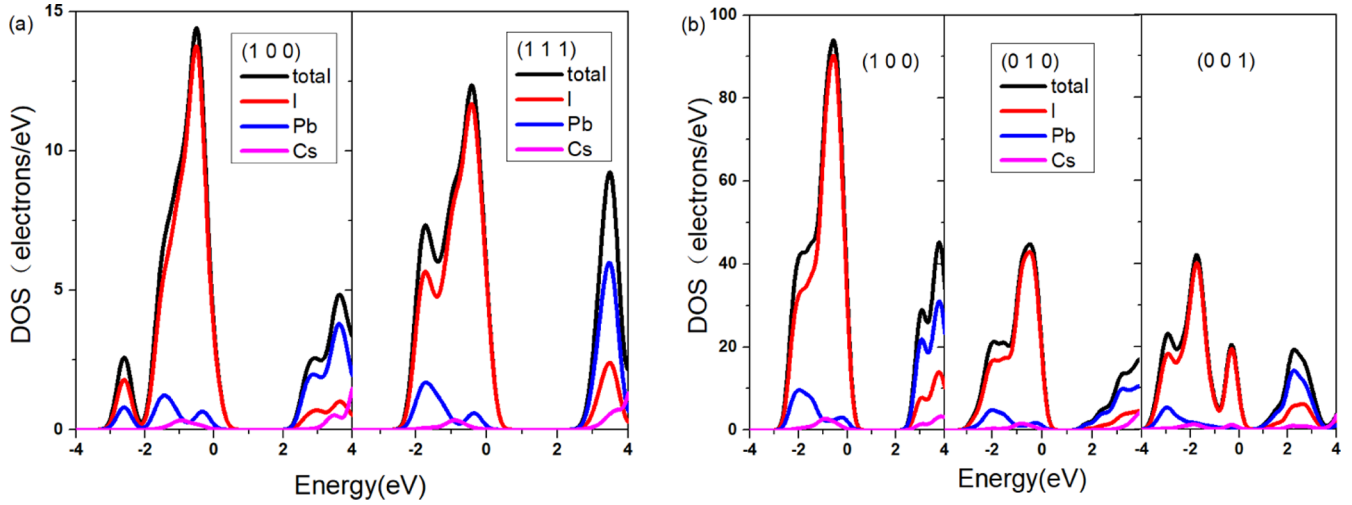

Figure 6. DOS of (a) (1 0 0) and (1 1 1) slices of the cubic structure and (b) (1 0 0), (0 1 0), and (1 1 1) slices of the orthogonal structure.

a flat band distribution and an increase in the band gap value. This theory is suitable for the cubic structure but cannot be explained for the orthogonal structure. We guess that maybe as the orthogonal structure is large, the system does not decrease much after being sliced. On the contrary, the interaction between the system becomes stronger. As can be seen from the band diagram shown in Figure 5, the band becomes steeper, indicating that the interaction between the atoms is enhanced after being sliced.

Figure 6 shows the DOS of the cubic and orthogonal structures after being sliced. It can be seen from Figure 6a that the DOS of the (1 0 0) and (1 1 1) surfaces of the cubic structure are very similar, while Figure 6b shows that the DOS of the orthogonal structure vary significantly after being sliced. According to the band diagram in Figure 5, the band of the (1 0 0) surface of the orthogonal structure near the Fermi surface is the densest, which is consistent with the DOS shown in Figure 6b. By analyzing the contribution of each element to the band diagram, it can be found that the conduction band is mostly contributed by Pb atoms, while the I atoms contribute a little, the valence band is almost contributed by I atoms, and the Cs atoms have no contribution to the electrons near the Fermi surface. This is similar to the DOS diagram of the uncut crystal.

We plot the partial charge density of the CBM and the VBM, as shown in Figures 7 and 8. It can be seen from Figures 7 and 8 that the charge density of the CBM is almost distributed around Pb atoms, while the charge density of the VBM is almost distributed around I atoms, which is consistent with the calculation results of PDOS.

3.3. Work Function. In order to better understand the photoelectric properties of $CsPbI_3$, we calculated the work function after being sliced. We know that the work function is the minimum energy that must be provided for an electron to escape from a solid surface. The work function is a physical quantity representing the binding energy of electrons, which is mainly affected by the type of elements and crystal structures. We use the optimized slices to calculate the work function and obtained it, as shown in Figure 9, the horizontal axis is the direction of the vacuum layer. It can be seen from Figure 9 that the work function of the (1 0 0) slice of the orthogonal structure is the largest, which is 5.558 eV, while the work function of the (1 1 1) slice of the cubic structure is the

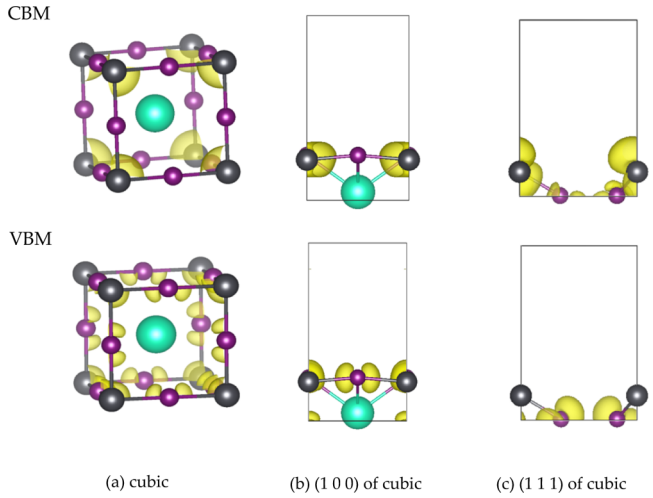

Figure 7. Partial charge densities of CBM and VBM of the cubic structure and sliced models.

smallest, which is 5.22 eV. It can be seen from the calculation results that the work function of each slice is between 5 and 6 eV, and there is not much difference. We compare the work functions of several metals, such as Ag: 4.26 eV, Al: 4.28 eV, Fe: 4.5 eV, Pb: 4.25 eV, and Pt: 5.65 eV. It is found that the work function of each slice of $CsPbI_3$ is between that of the other metals and Pt.

3.4. Carrier Mobility. The calculated data related to the carrier mobility of cubic and orthogonal structures are recorded in Table 2, and the mobility is calculated by formula 2. Table 2 shows that in the cubic structure, the effective mass of the electron is 0.33 m_0 in three directions, and their DP and elastic modulus in three directions are also the same, showing isotropy. We obtained that the electron mobility is 440 $cm^2\ V^{-1}\ S^{-1}$, which is consistent with the 430 $cm^2\ V^{-1}\ S^{-1}$ calculated by Ying *et al.*[41] Similarly, the effective mass, DP, and elastic modulus of the holes in the cubic structure are also the same in all the three directions, showing a high degree of isotropy. The calculated carrier mobility is 97 $cm^2\ V^{-1}\ S^{-1}$, which is consistent with the 80 $cm^2\ V^{-1}\ S^{-1}$ calculated by Poncé *et al.*[43] Compared with the cubic structure, the overall mobility of the orthogonal structure is lower. In particular, the mobility of both electrons and holes along the *x*-axis is almost

https://doi.org/10.1021/acsomega.1c00734
ACS Omega 2021, 6, 11545−11555

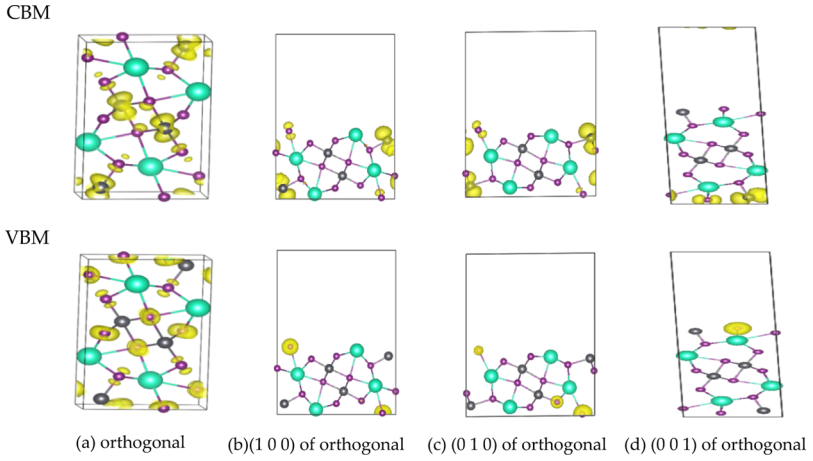

Figure 8. Partial charge densities of CBM and VBM of the orthogonal structure and sliced models.

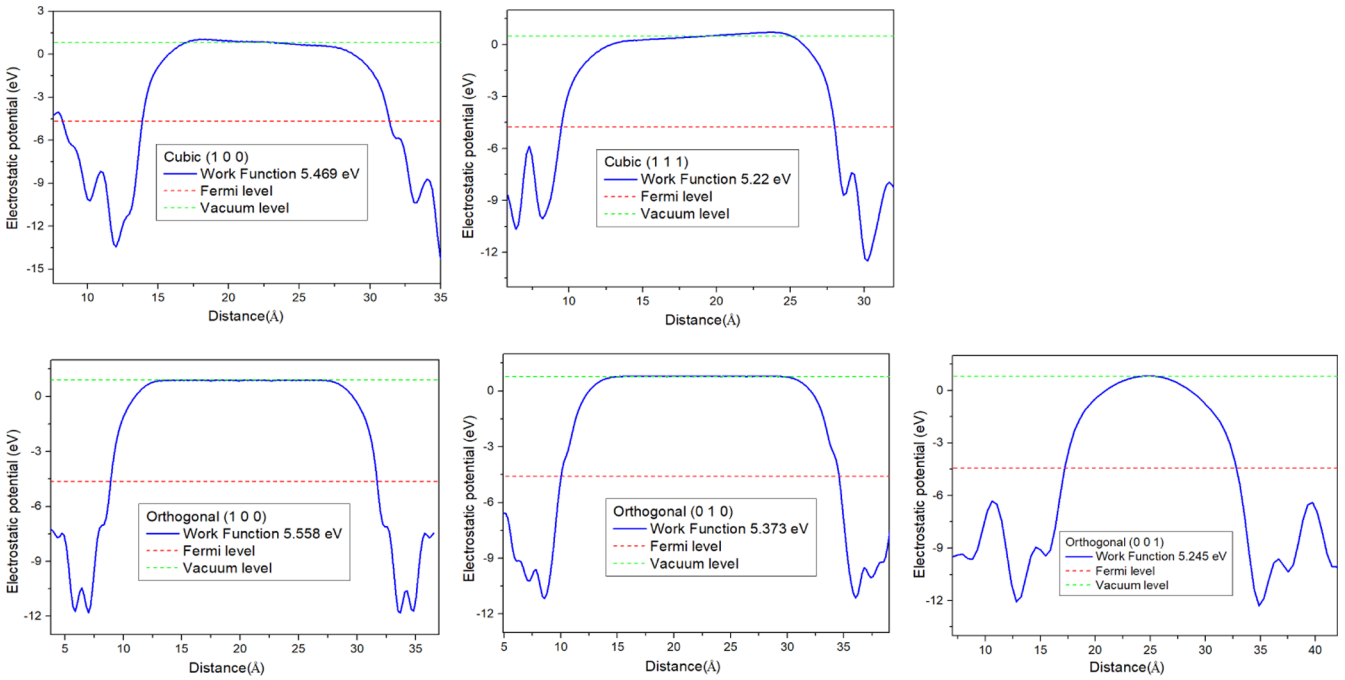

Figure 9. Work functions of slices of cubic and orthogonal structures.

Table 2. Carrier Mobility of Cubic and Orthogonal Structures Calculated by PBE with and without SOC

carrier type	m_x^*/m_0	m_y^*/m_0	m_z^*/m_0	E_{1x} (eV)	E_{1y} (eV)	E_{1z} (eV)	$C_{x/3D}$ (GPa)	$C_{y/3D}$ (GPa)	$C_{z/3D}$ (GPa)	$\mu_{x/3D}$ ($cm^2 V^{-1} S^{-1}$)	$\mu_{y/3D}$ ($cm^2 V^{-1} S^{-1}$)	$\mu_{z/3D}$ ($cm^2 V^{-1} S^{-1}$)
Without SOC Calculated by PBE												
e (cubic)	0.33	0.33	0.33	9	9	9	37.23	37.23	37.23	440	440	440
h (cubic)	0.36	0.36	0.36	17.28	17.28	17.28	37.23	37.23	37.23	97	97	97
e (orthogonal)	8.52	0.54	1.73	8.25	7.23	6.37	26.70	33.25	40.81	0.11	179	15
h (orthogonal)	3.96	2.25	0.85	15.24	16.79	9.24	26.70	33.25	40.81	0.22	1	43
With SOC Calculated by PBE												
e (cubic)	0.21	0.21	0.21	8.21	8.21	8.21	31.54	31.54	31.54	1399	1399	1399
h (cubic)	0.32	0.32	0.32	15.35	15.35	15.35	31.54	31.54	31.54	140	140	140
e (orthogonal)	8.50	0.62	1.82	8.53	7.67	7.02	24.26	30.18	35.22	0.10	102	10
h (orthogonal)	7.25	2.01	1.02	13.24	15.78	8.86	24.26	30.18	35.22	0.06	1	26

0 mainly because the effective mass of carriers in this direction is too large (it can be seen from the band diagram in Figure 2d that the band is almost flat from the direction of $G \rightarrow X$). In the orthogonal structure, the electron with the highest mobility along the y-axis is 179 $cm^2 V^{-1} S^{-1}$, while the hole only has a small mobility along the z-axis. The effective mass, DP, elastic modulus, and mobility all exhibit a high degree of anisotropy due to the poor symmetry of the orthogonal structure. It is found that the overall mobility of holes in both structures is lower than that of electrons mainly because the effective mass

https://doi.org/10.1021/acsomega.1c00734
ACS Omega 2021, 6, 11545−11555

Table 3. Carrier Mobility of (1 0 0) and (1 1 1) Surfaces of Cubic Structure and (1 0 0), (0 1 0), and (0 0 1) Surfaces of the Orthogonal Structure

carrier type	m_x^*/m_0	m_y^*/m_0	E_{1x} (eV)	E_{1y} (eV)	$C_{x/2D}$ (J m^{-2})	$C_{y/2D}$ (J m^{-2})	$\mu_{x/2D}$ (cm^2 V^{-1} S^{-1})	$\mu_{y/2D}$ (cm^2 V^{-1} S^{-1})
Cubic Structure								
e (1 0 0)	0.52	0.52	7.87	7.87	198.74	170.35	249	214
h (1 0 0)	0.57	0.57	9.33	9.33	198.74	170.35	148	126
e (1 1 1)	1.44	1.41	5.95	5.95	375.12	375.12	108	111
h (1 1 1)	4.70	6.02	11.54	11.54	375.12	375.12	2	1.8
Orthogonal Structure								
e (1 0 0)	0.25	0.25	6.35	6.75	98.36	105.21	820	776
h (1 0 0)	3.52	2.37	7.36	7.45	98.36	105.21	4	6
e (0 1 0)	1.38	1.38	8.21	8.45	89.35	94.28	15	15
h (0 1 0)	0.87	0.82	8.01	8.16	89.35	94.28	40	43
e (0 0 1)	0.53	2.35	7.85	7.69	116.25	121.35	67	16
h (0 0 1)	0.89	8.42	9.21	9.38	116.25	121.35	12	1

Table 4. Dielectric Constants (ε_s) and Exciton Binding Energy (E_b) Calculated by PBE[a]

crystal system	cubic	orthogonal	(1 0 0) of cubic	(1 1 1) of cubic	(1 0 0) of orthogonal	(0 1 0) of orthogonal	(0 0 1) of orthogonal
ε_s	4.81	4.25	4.46	4.37	3.16	3.37	3.14
$\overline{m_e^*}/m_0$	0.33	3.60	0.52	1.41	0.25	1.38	1.44
$\overline{m_h^*}/m_0$	0.36	2.35	0.57	5.36	2.81	0.85	4.67
E_b (meV)	101	1071	186	795	313	630	1519

[a]The effective mass of electrons and holes in the bulk and sliced models is the average effective mass in all directions. $\overline{m_e^*}$ and $\overline{m_h^*}$ are the average effective masses of electrons and holes in all directions.

and the DP of holes is greater than that of electrons. It is consistent with the usual findings in simple semiconductors.[51]

At the same time, we also analyze the carrier mobility after considering the SOC effect. After considering the SOC effect, the carrier mobility of the cubic structure increases obviously, but the orthogonal structure does have a tendency to decrease. In the cubic structure, the mobility of electrons increased from 440 to 1399 cm^2 V^{-1} S^{-1}, and the mobility of holes also increased from 97 to 140 cm^2 V^{-1} S^{-1}. In the orthogonal structure, the electron mobility along the y-axis decreases from 179 to 102 cm^2 V^{-1} S^{-1}. According to the band diagrams, as shown in Figure 2c,f, it can be found that the energy level splits after considering the SOC effect, and the CBM and VBM of the cubic structure become steeper after splitting, while those of the orthogonal structure tend to flatten slightly. The effective mass we calculated from Table 2 can more specifically reflect the change in trend of the band. After considering the SOC effect, the effective mass of the electron in the cubic structure is only 0.21 m_0 in all the three directions, less than the original 0.33 m_0, and the effective mass of the hole is also reduced from the original 0.36 to 0.32 m_0. In the orthogonal structure, the effective mass of the hole along the x-axis increases from 3.96 to 7.25 m_0, and the effective mass of the electron along the y-axis increases from 0.54 to 0.62 m_0.

Table 3 shows the carrier mobility of the cubic and orthogonal structures after being sliced, and the mobility is calculated by formula 1. We find that the overall carrier mobility is slightly improved after being sliced. In the cubic structure, the mobility of the electron on the (1 0 0) surface along the x-axis is 249 cm^2 V^{-1} S^{-1}, while the mobility of the hole on the (1 1 1) surface is only 2 cm^2 V^{-1} S^{-1}. The mobility of electrons and holes on the (1 0 0) surface of the cubic structure is relatively average, while the mobility on the (1 1 1) surface of the cubic structure is mainly concentrated on electrons. In the orthogonal structure, the mobility of the electrons on the (1 0 0) surface along the x-axis is the largest, which is 820 cm^2 V^{-1} S^{-1}, while the mobility of the holes on the (0 0 1) surface along the y-axis is only 1 cm^2 V^{-1} S^{-1}. The carrier mobility on the (1 0 0) surface is relatively high in the orthogonal structure, while on the other surfaces is very low, within 100 cm^2 V^{-1} S^{-1}. By comparing the data in Table 3, it can be found that the main factor affecting the carrier mobility is the effective mass of the carrier. For example, the effective mass of the holes on the (1 1 1) surface of the cubic structure along the x- and y-axes are 4.70 and 6.02 m_0 respectively, while the effective mass of the holes on the (0 0 1) surface of the orthogonal structure along the y-axis is even 8.42 m_0.

By analyzing the CBM and VBM of band diagrams of crystals, we find that all carriers with a flat band have low mobility, while carriers with a steep band have high mobility. We know that the effective mass of the carrier is inversely proportional to the second derivative of the band, so the steeper the band, the smaller the effective mass of the carrier, and the more conducive to the transport of the carrier. According to the knowledge of solid-state physics, we know that the steeper the band, the stronger the interaction between the atoms, making the charge distribution between the atoms more continuous. Combined with the partial charge density shown in Figures 7 and 8, we find that the charge distributions of the CBM and VBM of the cubic structure are more continuous, and the charge distribution of the CBM is more continuous than that of the VBM, which is conducive to carrier migration.

In order to better study the carrier mobility, we also calculate the exciton binding energy, and the calculated data are shown in Table 4. The exciton binding energy is obtained by the Wannier–Mott[57] formula

$$E_b = \frac{m_e m_h R_y}{m_0 (m_e + m_h) \varepsilon_s^2} \quad (3)$$

https://doi.org/10.1021/acsomega.1c00734
ACS Omega 2021, 6, 11545−11555

where, ε_s is the static dielectric constant, m_e and m_h are the average effective masses in all directions, and R_y = 13.6057 eV is the Rydberg energy constant. According to the data in Table 4, it can be found that the exciton binding energy in the cubic structure is only 101 meV, which is the easiest to separate and generate carriers, while the exciton binding energy in the (0 0 1) surface of the orthogonal structure is the highest, which is difficult to separate and affects the carrier mobility. All of them are consistent with the calculated results of carrier mobility.

3.5. Optical Absorption Coefficient. If the alignment of band energy levels between the light-absorber and charge extracting material is harmonious, a high absorption coefficient will lead to a high mobility.[58,59] Figure 10 shows the

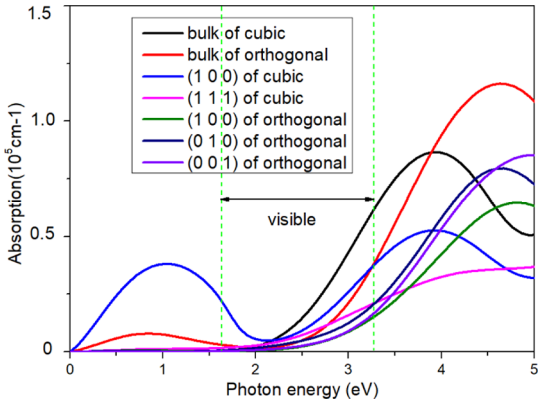

Figure 10. Optical absorption coefficient of structures and slices.

absorption coefficient of various structures as a function of photon energy. Figure 10 shows that the absorption coefficient at the absorption edge reaches 10^4–10^5 cm^{-1}, with a high absorption coefficient, which is close to the absorption coefficient of $MAPbI_3$ calculated by Wang *et al.*[40] The high absorption coefficient is due to the high density of Pb 6p states in the CBM and I 5p states in the VBM, as well as the transition of Pb 6s states at the VBM to Pb 6p states at the CBM. We divided the absorption light into visible light, infrared light, and ultraviolet light for analysis. In the range of visible light, the cubic structure had the highest absorption coefficient; in the range of infrared light, the (1 0 0) slice of the cubic structure had the highest absorption coefficient; in the range of ultraviolet light, the orthogonal structure had the highest absorption coefficient. This is consistent with the previous calculation of carrier mobility and exciton binding energy. Through further comparison of the absorption coefficient, mobility, and exciton binding energy, we found that $CsPbI_3$ has the highest utilization rate of visible light, followed by infrared, and very low utilization rate of ultraviolet light in the photoelectric conversion. The reasons are as follows: (i) the cubic bulk structure absorbs the most visible light, so the carrier mobility is the highest, and the exciton binding energy is the lowest. (ii) Although the orthogonal bulk structure absorbs the most ultraviolet light, the carrier mobility is not as high as that of the (1 0 0) surface of the cubic structure, and the exciton binding energy is relatively high. In order to better verify our conclusion, we compared the previously calculated data as follows: the maximum mobility of the orthogonal structure is 140 $cm^2\ V^{-1}\ S^{-1}$ and the exciton binding energy is 1071 meV; while the maximum mobility of the (1 0 0) surface of the cubic structure is 249 $cm^2\ V^{-1}\ S^{-1}$ and the exciton binding energy is 186 meV.

4. CONCLUSIONS

In this paper, the crystal structure and electronic properties of the cubic and orthogonal crystal systems of $CsPbI_3$ are analyzed, and their slices are similarly analyzed. According to the diagrams of DOS and partial charge density, it can be clearly found that the conduction band near the Fermi surface is mainly contributed by Pb atoms, while the valence band near the Fermi surface is mainly contributed by I atoms. By calculating the work function, it is found that the work function of each slice of $CsPbI_3$ is between other metals and Pt (between 5 and 6 eV), and the work function of each slice has little difference.

Then, we focus on the carrier mobility in several structures. First, the carrier mobility of the two bulks is studied. It is found that the mobility of the cubic bulk is higher than that of the orthogonal bulk. After considering the SOC effect, the carrier mobility of the cubic bulk structure increases obviously, but the orthogonal bulk structure does have a tendency to decrease. The electron mobility in the cubic structure is the highest after considering the SOC effect, reaching 1399 $cm^2\ V^{-1}\ S^{-1}$, which is equal to the Si-based, PbSe, and PbTe traditional solar cells[10,39] (μ_{Si} = 1400 $cm^2\ V^{-1}\ S^{-1}$, μ_{PbSe} = 1140$cm^2\ V^{-1}\ S^{-1}$, and μ_{PbTe} = 1508 $cm^2\ V^{-1}\ S^{-1}$). Then, we studied the mobility of the bulks after being sliced and found that the mobility increased a little. The mobility is mainly affected by the effective mass of the carrier and the DP. By calculating the exction binding energy, it is found that the exciton binding energy in the cubic structure is the lowest, while the exction binding energy in the (0 0 1) surface of the orthogonal structure is the highest, which is in good agreement with the calculated results of the carrier mobility.

Finally, we calculate their light absorption coefficient, the result shows that the light absorption coefficient is relatively high. In the visible region, the absorption coefficient of the cubic structure is the best and the carrier mobility is also the highest in all structures of $CsPbI_3$. In the infrared region, the best absorption is the (1 0 0) surface of the cubic structure, and the mobility is also high. In the ultraviolet region, the best absorption is the orthogonal bulk structure, while the mobility is not too high, which indicates that the solar cell material has a very low utilization rate of ultraviolet light.

This paper mainly analyzed the mobility and optical properties of $CsPbI_3$ and compared them with some other traditional solar cell materials and found that $CsPbI_3$ has the potential to be a high-efficiency solar cell material, which provides a certain theoretical basis for the later experimental preparation.

AUTHOR INFORMATION

Corresponding Author

Yan-Lin Tang − *College of Physics, Guizhou University, Guiyang 550025, China*; Email: tylgzu@163.com

Author

Li-Ke Gao − *College of Big Data and Information Engineering, Guizhou University, Guiyang 550025, China*; orcid.org/0000-0002-3127-5790

Complete contact information is available at: https://pubs.acs.org/10.1021/acsomega.1c00734

Notes

The authors declare no competing financial interest.

https://doi.org/10.1021/acsomega.1c00734
ACS Omega 2021, 6, 11545−11555

■ ACKNOWLEDGMENTS

This work was supported by the National Natural Science Foundation of China Program (grant no. 11164004 and 61835003 and the Industrial Research Project of Guizhou Province (GY[2012]3060).

■ REFERENCES

(1) Hagfeldt, A.; Boschloo, G.; Sun, L.; Kloo, L.; Pettersson, H. Dye-Sensitized Solar Cells. *Chem. Rev.* **2010**, *110*, 6595−6663.
(2) Burschka, J.; Pellet, N.; Moon, S.-J.; Humphry-Baker, R.; Gao, P.; Nazeeruddin, M. K.; Grätzel, M. Sequential deposition as a route to high-performance perovskite-sensitized solar cells. *Nature* **2013**, *499*, 316.
(3) Liu, M.; Johnston, M. B.; Snaith, H. J. Efficient planar heterojunction perovskite solar cells by vapour deposition. *Nature* **2013**, *501*, 395.
(4) Xiao, W. B.; Liu, M. M.; Yan, C. Extracting and Studying Solar Cell Five Parameters Based on Lambert W Function. *J. Nanoelectron. Optoelectron.* **2017**, *12*, 189−195.
(5) Park, H.-J.; Lee, K.-H.; Kumar, B.; Shin, K.-S.; Jeong, S.-W.; Kim, S.-W. Inverted Organic Solar Cells with ZnO Thin Films Prepared by Sol-Gel Method. *J. Nanoelectron. Optoelectron.* **2010**, *5*, 135−138.
(6) Yella, A.; Lee, H. W.; Tsao, H. N.; Yi, C. Y.; Chandiran, A. K. Porphyrin-sensitized solar cells with cobalt (II/III)-based redox electrolyte exceed 12 percent efficiency (vol 334, pg 629, 2011). *Science* **2011**, *334*, 629.
(7) Jeon, N. J.; Noh, J. H.; Yang, W. S.; Kim, Y. C.; Ryu, S.; Seo, J.; Seok, S. I. Compositional engineering of perovskite materials for high-performance solar cells. *Nature* **2015**, *517*, 476.
(8) Lee, M. M.; Teuscher, J.; Miyasaka, T.; Murakami, T. N.; Snaith, H. J. Efficient Hybrid Solar Cells Based on Meso-Superstructured Organometal Halide Perovskites. *Science* **2012**, *338*, 643−647.
(9) Chiang, C. H.; Nazeeruddin, M. K.; Gratzel, M.; Wu, C. G. The synergistic effect of H2O and DMF towards stable and 20% efficiency inverted perovskite solar cells. *Energy Environ. Sci.* **2017**, *10*, 808−817.
(10) Xie, M.; Zhang, S.; Cai, B.; Huang, Y.; Zou, Y.; Guo, B.; Gu, Y.; Zeng, H. A promising two-dimensional solar cell donor: Black arsenic−phosphorus monolayer with 1.54 eV direct bandgap and mobility exceeding 14,000 cm2V−1s−1. *Nano Energy* **2016**, *28*, 433−439.
(11) Jorgensen, M.; Norrman, K.; Krebs, F. C. Stability/degradation of polymer solar cells. *Sol. Energy Mater. Sol. Cells* **2008**, *92*, 686−714.
(12) Yoshikawa, K.; Kawasaki, H.; Yoshida, W.; Irie, T.; Konishi, K.; Nakano, K.; Uto, T.; Adachi, D.; Kanematsu, M.; Uzu, H.; Yamamoto, K. Silicon heterojunction solar cell with interdigitated back contacts for a photoconversion efficiency over 26%. *Nat. Energy* **2017**, *2*, 17032.
(13) Kelzenberg, M. D.; Boettcher, S. W.; Petykiewicz, J. A.; Turner-Evans, D. B.; Putnam, M. C.; Warren, E. L.; Spurgeon, J. M.; Briggs, R. M.; Lewis, N. S.; Atwater, H. A. Enhanced absorption and carrier collection in Si wire arrays for photovoltaic applications. *Nat. Mater.* **2010**, *9*, 239−244.
(14) Bang, J. H.; Kamat, P. V. Quantum Dot Sensitized Solar Cells. A Tale of Two Semiconductor Nanocrystals: CdSe and CdTe. *ACS Nano* **2009**, *3*, 1467−1476.
(15) Pan, Z.; Zhao, K.; Wang, J.; Zhang, H.; Feng, Y.; Zhong, X. Near Infrared Absorption of CdSexTe1-x, Alloyed Quantum Dot Sensitized Solar Cells with More than 6% Efficiency and High Stability. *ACS Nano* **2013**, *7*, 5215.
(16) Kojima, A.; Teshima, K.; Shirai, Y.; Miyasaka, T. Organometal Halide Perovskites as Visible-Light Sensitizers for Photovoltaic Cells. *J. Am. Chem. Soc.* **2009**, *131*, 6050.
(17) https://www.nrel.gov/pv/cell-efficiency.html. Accessed in 2020.
(18) Ku, Z. L.; Rong, Y. G.; Xu, M.; Liu, T. F.; Han, H. W. Full Printable Processed Mesoscopic CH3NH3PbI3/TiO2 Heterojunction Solar Cells with Carbon Counter Electrode. *Sci. Rep.* **2013**, *3*, 3132.
(19) Kim, H. S.; Lee, C. R.; Im, J. H.; Lee, K. B.; Moehl, T.; Marchioro, A.; Moon, S. J.; Humphry-Baker, R.; Yum, J. H.; Moser, J. E.; Grätzel, M.; Park, N. G. Lead Iodide Perovskite Sensitized All-Solid-State Submicron Thin Film Mesoscopic Solar Cell with Efficiency Exceeding 9%. *Sci. Rep.* **2012**, *2*, 591.
(20) Snaith, H. J. Perovskites: The Emergence of a New Era for Low-Cost, High-Efficiency Solar Cells. *J. Phys. Chem. Lett.* **2013**, *4*, 3623−3630.
(21) Katan, C.; Mercier, N.; Even, J. Quantum and Dielectric Confinement Effects in Lower-Dimensional Hybrid Perovskite Semiconductors. *Chem. Rev.* **2019**, *119*, 3140−3192.
(22) Tan, Z.-K.; Moghaddam, R. S.; Lai, M. L.; Docampo, P.; Higler, R.; Deschler, F.; Price, M.; Sadhanala, A.; Pazos, L. M.; Credgington, D.; Hanusch, F.; Bein, T.; Snaith, H. J.; Friend, R. H. Bright light-emitting diodes based on organometal halide perovskite. *Nat. Nanotechnol.* **2014**, *9*, 687−692.
(23) Qiu, J.; Qiu, Y.; Yan, K.; Zhong, M.; Mu, C.; Yan, H.; Yang, S. All-solid-state hybrid solar cells based on a new organometal halide perovskite sensitizer and one-dimensional TiO2 nanowire arrays. *Nanoscale* **2013**, *5*, 3245−3248.
(24) Lang, L.; Yang, J.-H.; Liu, H.-R.; Xiang, H. J.; Gong, X. G. First-principles study on the electronic and optical properties of cubic ABX(3) halide perovskites. *Phys. Lett. A* **2014**, *378*, 290−293.
(25) Murtaza, G.; Ahmad, I. First principle study of the structural and optoelectronic properties of cubic perovskites CsPbM3 (M=Cl, Br, I). *Phys. B* **2011**, *406*, 3222−3229.
(26) Jing, H.; Sa, R.; Xu, G. Tuning electronic and optical properties of CsPbI3 by applying strain: A first-principles theoretical study. *Chem. Phys. Lett.* **2019**, *732*, 136642.
(27) Pauling, L. The Principles Determining the Structure of Complex Ionic Crystals. *J. Am. Chem. Soc.* **1929**, *51*, 1010−1026.
(28) Fadla, M. A.; Bentria, B.; Dahame, T.; Benghia, A. First-principles investigation on the stability and material properties of all-inorganic cesium lead iodide perovskites CsPbI3 polymorphs. *Phys. B* **2020**, *585*, 412118.
(29) Sutton, R. J.; Filip, M. R.; Haghighirad, A. A.; Sakai, N.; Wenger, B.; Giustino, F.; Snaith, H. J. Cubic or Orthorhombic? Revealing the Crystal Structure of Metastable Black-Phase CsPbI(3) by Theory and Experiment. *ACS Energy Lett.* **2018**, *3*, 1787−1794.
(30) Sanchez, S.; Christoph, N.; Grobety, B.; Phung, N.; Steiner, U.; Saliba, M.; Abate, A. Efficient and Stable Inorganic Perovskite Solar Cells Manufactured by Pulsed Flash Infrared Annealing. *Adv. Energy Mater.* **2018**, *8*, 1802060.
(31) Eperon, G. E.; Paternò, G. M.; Sutton, R. J.; Zampetti, A.; Haghighirad, A. A.; Cacialli, F.; Snaith, H. J. Inorganic caesium lead iodide perovskite solar cells. *J. Mater. Chem. A* **2015**, *3*, 19688−19695.
(32) Stoumpos, C. C.; Malliakas, C. D.; Kanatzidis, M. G. Semiconducting Tin and Lead Iodide Perovskites with Organic Cations: Phase Transitions, High Mobilities, and Near-Infrared Photoluminescent Properties. *Inorg. Chem.* **2013**, *52*, 9019−9038.
(33) Zhang, T. Y.; Dar, M. I.; Li, G.; Xu, F.; Guo, N. J.; Gratzel, M.; Zhao, Y. X. Bication lead iodide 2D perovskite component to stabilize inorganic alpha-CsPbI3 perovskite phase for high-efficiency solar cells. *Sci. Adv.* **2017**, *3*, No. e1700841.
(34) Hoffman, J. B.; Schleper, A. L.; Kamat, P. V. Transformation of Sintered CsPbBr3 Nanocrystals to Cubic CsPbI3 and Gradient CsPbBrxI3-x through Halide Exchange. *J. Am. Chem. Soc.* **2016**, *138*, 8603−8611.
(35) Steele, J. A.; Jin, H.; Dovgaliuk, I.; Berger, R. F.; Braeckevelt, T.; Yuan, H.; et al. Thermal unequilibrium of strained black CsPbI3 thin films. *Science* **2019**, *365*, 679.
(36) Qiao, J.; Kong, X.; Hu, Z. X.; Yang, F.; Ji, W. High-mobility transport anisotropy and linear dichroism in few-layer black phosphorus. *Nat. Commun.* **2014**, *5*, 4475.
(37) Fei, R.; Yang, L. Strain-engineering the anisotropic electrical conductance of few-layer black phosphorus. *Nano Lett.* **2014**, *14*, 2884−2889.

https://doi.org/10.1021/acsomega.1c00734
ACS Omega 2021, 6, 11545−11555

(38) Xie, J.; Zhang, Z. Y.; Yang, D. Z.; Xue, D. S.; Si, M. S. Theoretical Prediction of Carrier Mobility in Few-Layer BC2N. *J. Phys. Chem. Lett.* **2014**, *5*, 4073−4077.
(39) Jong, U.-G.; Yu, C.-J.; Kye, Y.-H.; Hong, S.-N.; Kim, H.-G. Manifestation of the thermoelectric properties in Ge-based halide perovskites. *Phys. Rev. Mater.* **2020**, *4*, 075403.
(40) Wang, Y.; Zhang, Y.; Zhang, P.; Zhang, W. High intrinsic carrier mobility and photon absorption in the perovskite CH3NH3PbI3. *Phys. Chem. Chem. Phys.* **2015**, *17*, 11516−11520.
(41) Ying, Y.; Luo, X.; Huang, H. Pressure-Induced Topological Nontrivial Phase and Tunable Optical Properties in All-Inorganic Halide Perovskites. *J. Phys. Chem. A* **2018**, *122*, 17718−17725.
(42) Lee, J.-H.; Deng, Z.; Bristowe, N. C.; Bristowe, P. D.; Cheetham, A. K. The competition between mechanical stability and charge carrier mobility in MA-based hybrid perovskites: insight from DFT. *J. Mater. Chem. C* **2018**, *6*, 12252−12259.
(43) Poncé, S.; Schlipf, M.; Giustino, F. Origin of Low Carrier Mobilities in Halide Perovskites. *ACS Energy Lett.* **2019**, *4*, 456−463.
(44) Kresse, G.; Furthmüller, J. Efficient iterative schemes for ab initio total-energy calculations using a plane-wave basis set. *Phys. Rev. B: Condens. Matter Mater. Phys.* **1996**, *54*, 11169−11186.
(45) Troullier, N.; Martins, J. L. Efficient pseudopotentials for plane-wave calculations. *Phys. Rev. B: Condens. Matter Mater. Phys.* **1991**, *43*, 1993−2006.
(46) Blöchl, P. E.; Jepsen, O.; Andersen, O. K. Improved Tetrahedron Method for Brillouin-Zone Integrations. *Phys. Rev. B: Condens. Matter Mater. Phys.* **1994**, *49*, 16223−16233.
(47) Even, J.; Pedesseau, L.; Jancu, J.-M.; Katan, C. Importance of Spin-Orbit Coupling in Hybrid Organic/Inorganic Perovskites for Photovoltaic Applications. *J. Phys. Chem. Lett.* **2013**, *4*, 2999−3005.
(48) Giorgi, G.; Fujisawa, J.-i.; Segawa, H.; Yamashita, K. Unraveling the adsorption mechanism of aromatic and aliphatic diols on the TiO2 surface: a density functional theory analysis. *Phys. Chem. Chem. Phys.* **2013**, *15*, 9761−9767.
(49) Kaasbjerg, K.; Thygesen, K. S.; Jauho, A.-P. Acoustic phonon limited mobility in two-dimensional semiconductors: Deformation potential and piezoelectric scattering in monolayer MoS2 from first principles. *Phys. Rev. B: Condens. Matter Mater. Phys.* **2013**, *87*, 235312.
(50) Kaasbjerg, K.; Thygesen, K. S.; Jacobsen, K. W. Phonon-limited mobility in n-type single-layer MoS2 from first principles. *Phys. Rev. B: Condens. Matter Mater. Phys.* **2012**, *85*, 115317.
(51) Bardeen, J.; Shockley, W. Deformation Potentials and Mobilities in Non-Polar Crystals. *Phys. Rev.* **1950**, *80*, 72−80.
(52) Trots, D. M.; Myagkota, S. V. High-temperature structural evolution of caesium and rubidium triiodoplumbates. *J. Phys. Chem. Solids* **2008**, *69*, 2520−2526.
(53) Sutton, R. J.; Filip, M. R.; Abbas, H. A.; Nobuya, S.; Bernard, W.; Feliciano, G.; Snaith, H. J. Cubic or Orthorhombic? Revealing the Crystal Structure of Metastable Black-phase CsPbI3 by Theory and Experiment. *ACS Energy Lett.* **2018**, *8*, 1787.
(54) Brivio, F.; Butler, K. T.; Walsh, A.; van Schilfgaarde, M. Relativistic quasiparticle self-consistent electronic structure of hybrid halide perovskite photovoltaic absorbers. *Phys. Rev. B: Condens. Matter Mater. Phys.* **2014**, *89*, 155204.
(55) Goldschmidt, V. M. DieGesetzeDerKrystallochemie. *Naturwissenschaften* **1926**, *14*, 477−485.
(56) Li, C.; Lu, X.; Ding, W.; Feng, L.; Gao, Y.; Guo, Z. Formability of ABX(3) (X = F, Cl, Br, I) halide perovskites. *Acta Crystallogr., Sect. B: Struct. Sci.* **2008**, *64*, 702−707.
(57) Rodina, A. V.; Dietrich, M.; Göldner, A.; Eckey, L.; Meyer, B. K. Free excitons in wurtzite GaN. *Phys. Rev. B: Condens. Matter Mater. Phys.* **2001**, *64*, 115204.
(58) Chen, Z.; Wang, J. J.; Ren, Y. H.; Yu, C. L.; Shum, K. Schottky solar cells based on CsSnI3 thin-films. *Appl. Phys. Lett.* **2012**, *101*, 093901.
(59) Kumar, M. H.; Dharani, S.; Leong, W. L.; Boix, P. P.; Prabhakar, R. R.; Baikie, T.; Shi, C.; Ding, H.; Ramesh, R.; Asta, M.; Graetzel, M.; Mhaisalkar, S. G.; Mathews, N. Lead-Free Halide Perovskite Solar Cells with High Photocurrents Realized Through Vacancy Modulation. *Adv. Mater.* **2014**, *26*, 7122.

https://doi.org/10.1021/acsomega.1c00734
ACS Omega 2021, 6, 11545−11555